Proceedings of the
Annual Stability Conference
Structural Stability Research Council
Atlanta, Georgia, April 21-24, 2020

Lateral-torsional deformations of C-section and Z-section beams with continuous bracing

Raymond H. Plaut[1], Cristopher D. Moen[2]

Abstract
Simply-supported, single-span, C-section and Z-section cold-formed steel beams subjected to a uniformly distributed load on the top flange are analyzed. Both gravity loading and wind uplift are considered. Continuous elastic restraints resist bending and twisting. The lateral restraint acts on the top flange. It is assumed that the thin-walled beams are linearly elastic and that the cross section maintains its shape during deformation. Lateral-torsional deformation for the C-section beam involves twist and bending in the weak direction. For the Z-section beam, the deformation involves coupling between bending in both the weak and strong directions, along with the twist. The governing equilibrium equations are solved numerically. The problem is motivated largely by roof purlins in metal buildings. Numerical results demonstrate the effects of load magnitude, bending and twisting restraint stiffnesses, and roof slope (with top flange facing either upslope or downslope). Finally, lateral-torsional buckling for particular loadings is discussed.

1. Introduction

This study is concerned with the deformation of partially restrained C-section and Z-section purlins and girts. Applications include metal building roof and wall systems, with through-fastened roofs (walls) or standing-seam roofs, subjected to gravity (pressure) or uplift (suction) loading (Yang and Bai 2017). The resultant loading on the purlin or girt acts eccentrically on a flange, causing translation, bending, and twist. Distortion of the cross section is neglected. The concept of buckling is discussed at the end of the paper.

Restrained Z-section and C-section beams under gravity and/or uplift loading have been analyzed and/or tested in a number of investigations, including Ye et al. (2002, 2004), Li (2004), Chu et al. (2004, 2005, 2006), Seek and Murray (2008), Li et al. (2012), Ren et al. (2012, 2016), Wu et al. (2014), Zhao et al. (2014), Zhu et al. (2014), Gajdzicki and Goczek (2015), Gosowski et al. (2015), Zhang and Tong (2016), Seek and Escobales (2016), and Bai et al. (2018). Values of the rotational stiffness are determined or used in Lucas et al. (1997), EN 1993-1-3 (2006), Vrany (2006), Katnam et al. (2007a, 2007b, 2008), Li et al. (2012), Gao and Moen (2012, 2014), Ren et al. (2012, 2016), Kujawa and Szymczak (2014), Wu et al. (2014), Yuan et al. (2014), Gajdzicki and Goczek (2015), Penava et al. (2015), Seek and Escobales (2016), Balázs and Melcher (2017),

[1]D. H. Pletta Professor of Engineering (Emeritus), Virginia Tech <rplaut@vt.edu>
[2]RunToSolve <cris.moen@runtosolve.com>

Balázs et al. (2017), Lei and Li (2017), Bai et al. (2018), Gajdzicki (2018), Tang et al. (2018), and Wang et al. (2018).

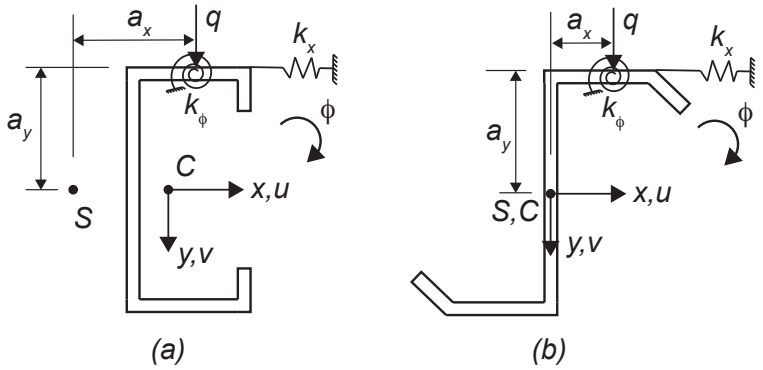

Figure 1: Cross sections: (a) C section; (b) Z section

In previous work with distributed elastic restraints, the authors analyzed the flexural-torsional deformations of elastic columns having initial crookedness and twist (Plaut and Moen 2019). Examples of compressed C-section, T-section, and I-section columns were considered there, and the effects of axial load, bracing stiffness, and relative orientations of the imperfections were investigated.

The analysis will be presented in Section 2. For no roof slope, results for Example 1, involving a beam with a C-section, will be described in Section 3, followed by results for Example 2, where the beam has a Z-section, in Section 4. The effect of roof slope on both examples will be discussed in Section 5. In Section 6, the concept of a critical load for a different application of the load in the two examples will be discussed, followed by concluding remarks in Section 7.

2. Formulation

In the cross sections in Fig. 1 (with no roof slope), the centroid is denoted C and the shear center is denoted S. The centroidal coordinate axes are x (horizontal) and y (vertical). The axis along the centroids is z (into the page in Fig. 1), with $0 \leq z \leq L$. The load is modeled as a uniformly distributed load q applied at the center of the top flange, with q positive for gravity loading and negative for uplift loading. The distances from the shear center to the point of application of q are a_x parallel to the x axis and a_y parallel to the y axis.

The single-span beam is assumed to be uniform and linearly elastic. It has length L, modulus of elasticity E, shear modulus G, moments of inertia I_x and I_y about the centroid, product of inertia I_{xy}, torsion constant J, and warping constant C_w. The weight of the beam is neglected.

The continuous bracing is linearly elastic. It has rotational stiffness k_ϕ per unit length along the z axis, and lateral stiffness k_x per unit length resisting translation parallel to the x axis and acting at the top of the top flange (see Fig. 1).

The deflections of the centroid along the x and y axes are $u(z)$ and $v(z)$, respectively, and the twist is $\phi(z)$, positive if clockwise in Fig. 1. It is assumed that deformations are small, with

$1+(u')^2 \approx 1, 1+(v')^2 \approx 1$, $sin\phi \approx \phi$, and $cos\phi \approx 1$.

When the roof has a slope, the slope angle is denoted θ, as shown in Fig. 2 (Seek and Murray 2008, Seek and Escobales 2016). If $\theta > 0$, the top flange faces upslope; if $\theta < 0$, the top flange faces downslope. The components of q along the positive x and y axes are denoted q_x and q_y, respectively, and are given by

$$q_y = qcos\theta, q_x = -qsin\theta. \tag{1}$$

When there is no roof slope, $\theta = 0$, $q_x = 0$, and $q_y = q$.

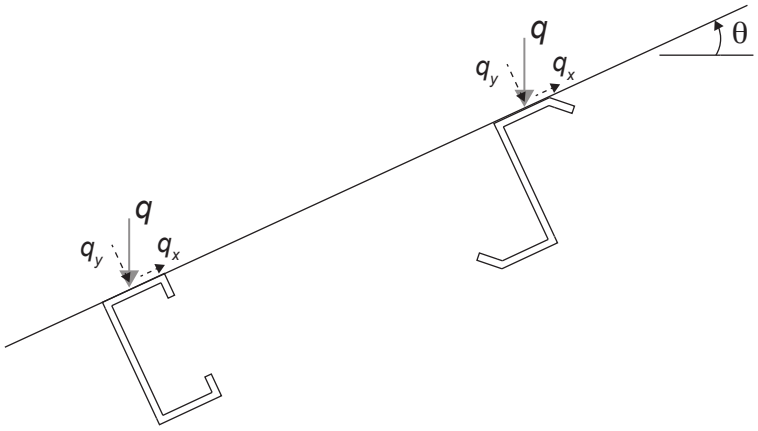

Figure 2: Cross sections with roof slope θ

The governing equilibrium equations are as follows:

$$EI_y u'''' + EI_{xy} v'''' + k_x(u + a_y\phi) = q_x, \tag{2}$$

$$EI_x v'''' + EI_{xy} u'''' = q_y, \tag{3}$$

$$EC_w\phi''''-GJ\phi'' + k_x a_y(u + a_y\phi) + k_\phi\phi = q_x(a_y-a_x\phi) + q_y(a_x + a_y\phi), \tag{4}$$

where primes denote differentiation with respect to z.

Some papers (e.g., Li et al. 2012, Ren et al. 2012, Bai et al. 2018) are missing the terms on the right-hand side of Eq. (4) that involve ϕ. Papers with such terms include Khelil and Larue (2008) and Gosowski et al. (2015).

One can eliminate v by solving Eq. (3) for v'''' and substituting the result into Eq. (2), giving

$$E(I_x I_y - I_{xy}^2)u'''' + k_x I_x(u + a_y\phi) = q_x I_x - q_y I_{xy}. \tag{5}$$

The ends of the beam are assumed to be simple supports (pinned), free to warp and to rotate about the x and y axes, but not allowed to rotate about the z axis or to deflect in the x and y directions.

The boundary conditions at the ends $z = 0$ and $z = L$ are $u = u'' = v = v'' = \phi = \phi'' = 0$.

Equations (2)-(4), or (4) and (5), along with the boundary conditions, can be solved analytically, but the solution is not simple (unless $k_x = 0$). Here numerical results are obtained by solving the boundary value problem using a shooting method with the subroutines NDSolve and FindRoot in Mathematica (e.g., Virgin et al. 2018). (If the symmetry of the displacements is utilized and the analysis is conducted from $z = 0$ to $z = L/2$, the conditions at $z = L/2$ are $u' = u''' = v' = v''' = \phi' = \phi''' = 0$.) Equations (2)-(4) were also recently used to numerically calculate the gravity and uplift load-deformation response of a 4-span continuous purlin supporting a standing seam roof (Moen 2020).

3. Example 1 (C Section) with No Roof Slope

The first example is a cold-formed steel stud beam with singly symmetric 9CS2.5x059 C cross section (AISI 2017) (see Fig. 1(a)). The beam is assumed to have L = 7620 mm (25 ft), $I_x = 4.287 \times 10^6$ mm^4 (10.3 in.^{4}), I_y = 290,500 mm^4 (0.698 in.^{4}), I_{xy} = 0, J = 424.56 mm^4 (0.00102 in.^{4}), $C_w = 3.1956 \times 10^9$ mm^6 (11.9 in.^{6}), E = 200 kN/mm^2 (29,000 kip/in.^{2}), $G = E/2.6$, a_x = 57.67 mm (2.27 in.), and a_y = 114.3 mm (4.5 in.).

Since I_{xy} = 0, Eq. (3) becomes uncoupled from Eqs. (2) and (4), and lateral-torsional deformation involves twist ϕ and deflection u in the weak direction. A typical shape of the twist $\phi(z)$ is shown by the solid curve in Fig. 3, which corresponds to the case q = 1 kN/m, k_x = 0.1 N/mm^2, and k_ϕ = 1000 N/rad.

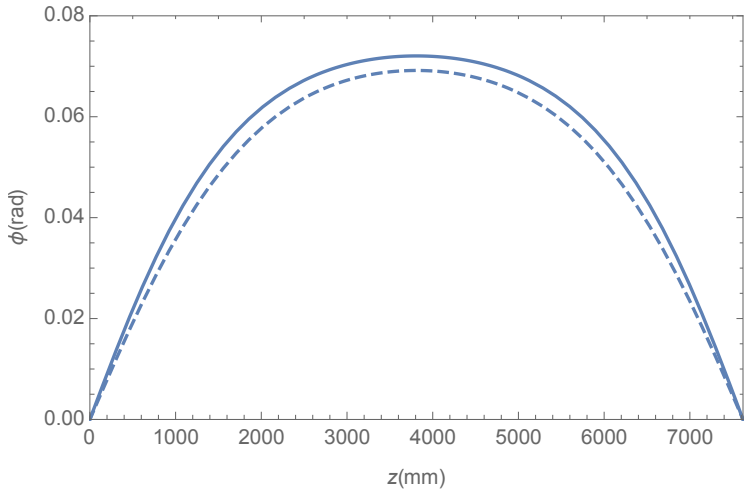

Figure 3: Shapes of twist for q = 1 kN/m, k_x = 0.1 N/mm^2, and k_ϕ = 1000 N/rad for Example 1 (solid) and Example 2 (dashed)

In all the following figures, the load q will be plotted as a function of the twist $\phi(L/2)$ at the center of the beam, which will usually have the maximum twist magnitude. For gravity loading, q and $\phi(L/2)$ will be positive, and for uplift loading they will be negative.

The case $k_x = 0$ is considered in Fig. 4 for gravity loading and in Fig. 5 for uplift loading. Curves for k_ϕ = 0, 100, 200, 300, 400, and 500 N/rad are presented. As k_ϕ increases, the load magnitude

corresponding to a given twist magnitude increases. In Fig. 4, as the load increases, the slope of each curve decreases. In Fig. 5, as the load magnitude increases, the magnitude of the slope of each curve increases. The range of q is 0 to 2 kN/m in Fig. 4, and –14 kN/m to 0 in Fig. 5. Due to these different ranges, the two figures are not combined over the total range –0.4 rad $\leq \phi \leq$ 0.4 rad.

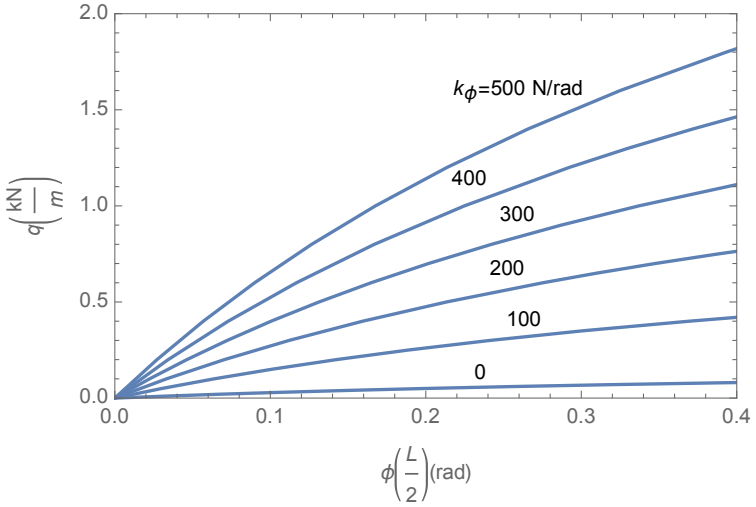

Figure 4: Gravity load versus central twist for Example 1 with $k_x = 0$

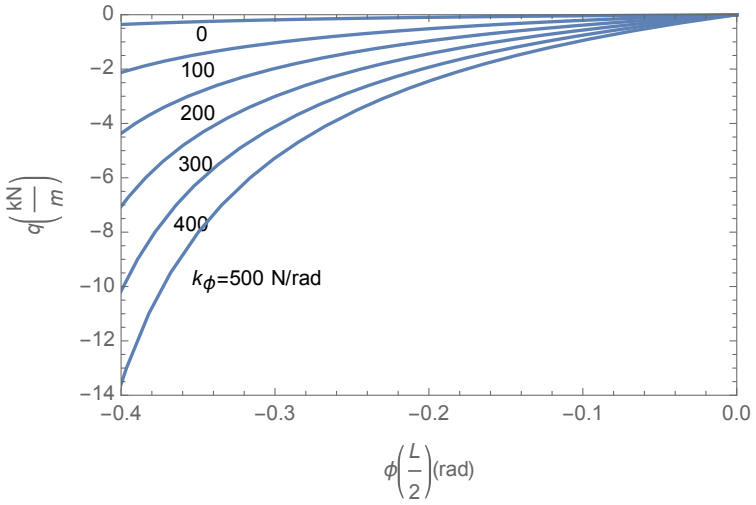

Figure 5: Uplift load versus central twist for Example 1 with $k_x = 0$

Similar results for the case $k_x = 0.1$ N/mm^2 are presented in Figs. 6 and 7. The values of k_ϕ are now 250, 500, 750, 1000, 1250, and 1500 N/rad. The range of q is 0 to 6 kN/m in Fig. 6, and –50 kN/m to 0 in Fig. 7.

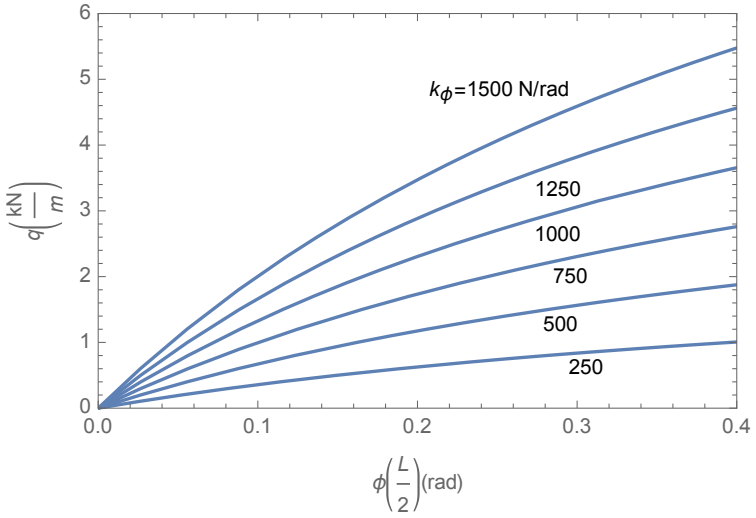

Figure 6: Gravity load versus central twist for Example 1 with k_x = 0.1 N/mm^2

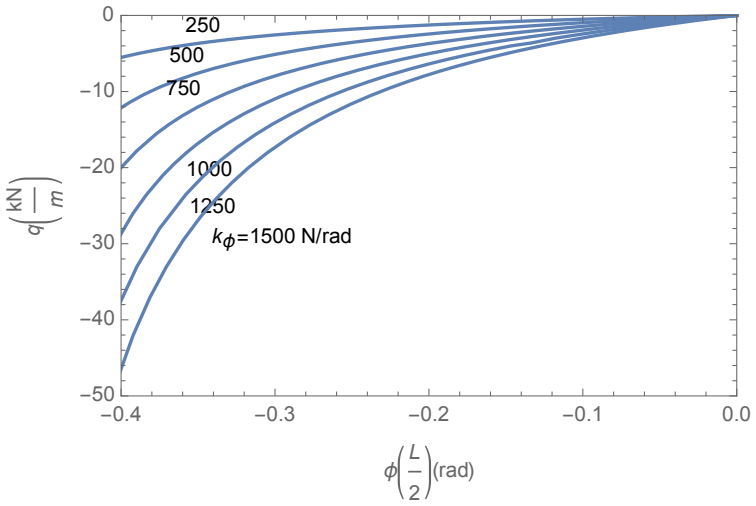

Figure 7: Uplift load versus central twist for Example 1 with k_x = 0.1 N/mm^2

In Figs. 8 and 9, the rotational stiffness k_ϕ = 0, and curves are plotted for k_x = 0, 0.001, 0.003, 0.01, and 0.1 N/mm^2. Curves for $k_x > 0.1$ N/mm^2 would be almost the same as the curves for k_x = 0.1 N/mm^2. The range of q is 0 to 0.16 kN/m in Fig. 8, and –0.7 kN/m to 0 in Fig. 9.

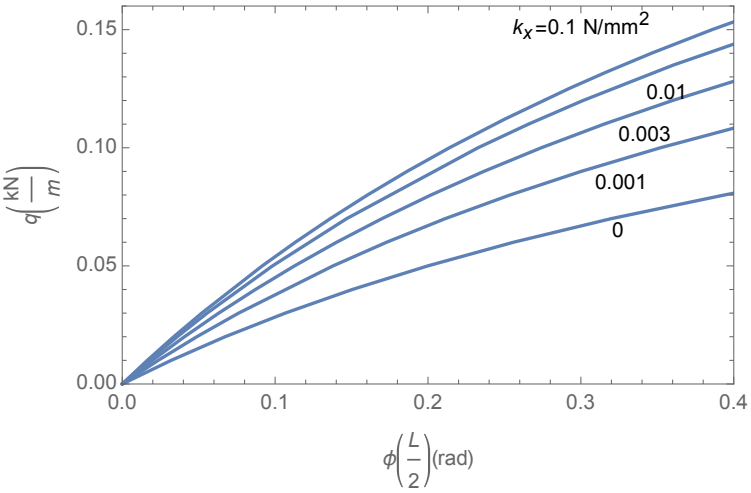

Figure 8: Gravity load versus central twist for Example 1 with $k_\phi = 0$

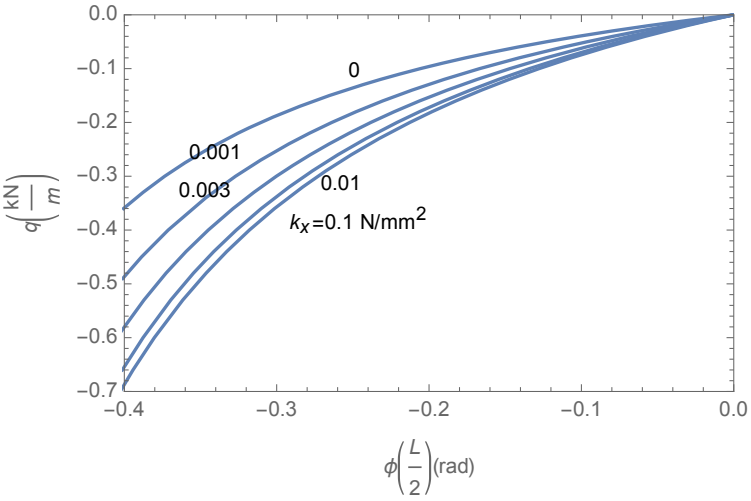

Figure 9: Uplift load versus central twist for Example 1 with $k_\phi = 0$

Finally, the case k_ϕ =1000 N/rad is treated in Figs. 10 and 11. In Fig. 10 for gravity loading, the curve for $k_x = 0$ (dashed) is almost the same as the curve for $k_x = 0.1$ N/mm^2 (solid). For uplift loading in Fig. 11, the curves separate perceptibly as the load magnitude decreases past $q = -8$ kN/m. The range of q is 0 to 4 kN/m in Fig. 10, and –35 kN/m to 0 in Fig. 11. Again, curves for $k_x > 0.1$ N/mm^2 would be almost the same as the curve for $k_x = 0.1$ N/mm^2, so changes in k_x do not have a large influence on the twist in Example 1 when k_ϕ =1000 N/rad.

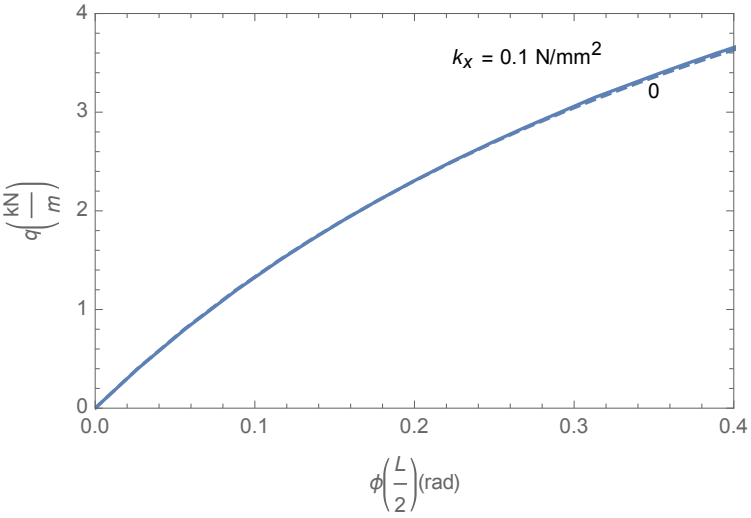

Figure 10: Gravity load versus central twist for Example 1 with k_ϕ = 1000 N/rad

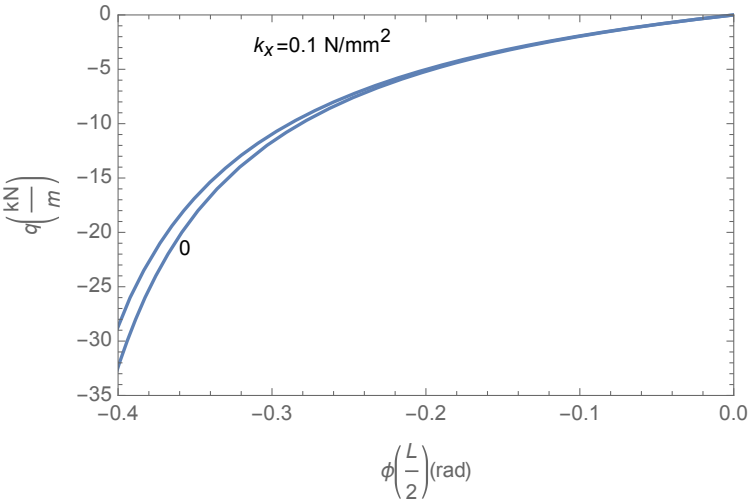

Figure 11: Uplift load versus central twist for Example 1 with k_ϕ = 1000 N/rad

Even though the vertical deflection $v(z)$ is independent of the lateral-torsional displacements, it is noted that for Example 1 the maximum magnitude of the slope $v'(z)$, occurring at the ends of the beam, is larger than 0.3 if the magnitude of q is larger than 13.95. Hence the lower portions of some of the curves in Figs. 7 and 11 do not satisfy the assumption of small slopes with respect to vertical deflection.

4. Example 2 (Z Section) with No Roof Slope

The second example is a cold-formed steel beam with 8ZS2.25x059 Z cross section (AISI 2017) (see Fig 1(b)).

The beam has L = 7620 mm (25 ft), $I_x = 3.230 \times 10^6$ mm^4 (7.76 in.^{4}), I_y = 449,530 mm^4 (1.08 in.^{4}), I_{xy} = 865,760 mm^4 (2.08 in.^{4}), J = 397.09 mm^4 (0.000954 in.^{4}), $C_w = 3.4104 \times 10^9$ mm^6

(12.7 in.[6]), E = 200 kN/mm^2 (29,000 kip/in.^{2}), $G = E/2.6$, a_x = 27.826 mm (1.096 in.), and a_y = 101.6 mm (4.0 in.). During uplift, the line of action of q passes through the shear center when ϕ = –0.278 rad.

Since $I_{xy} \neq 0$, the deformation involves the deflections u and v in the weak and strong directions, respectively, along with the twist ϕ. A typical shape of the twist $\phi(z)$ is shown by the dashed curve in Fig. 3, which corresponds to the case q = 1 kN/m, k_x = 0.1 N/mm^2, and k_ϕ = 1000 N/rad.

Figs. 12 and 13 depict results for the case $k_x = 0$ under gravity and uplift loading, respectively, with k_ϕ = 0, 100, 200, 300, 400, and 500 N/rad. The range of q is 0 to 3 kN/m in Fig. 12, and –3 kN/m to 0 in Fig. 13.

In Figs. 12, 13, 17, 19, and 20, when the maximum slope magnitude $|u'(0)|$ of the lateral deflection is larger than 0.3, the curve is dashed. Hence, due to the assumption of small slopes, these dashed portions may not be reliable. In Fig. 13, the dashed portions begin at q = –2.64 kN/m.

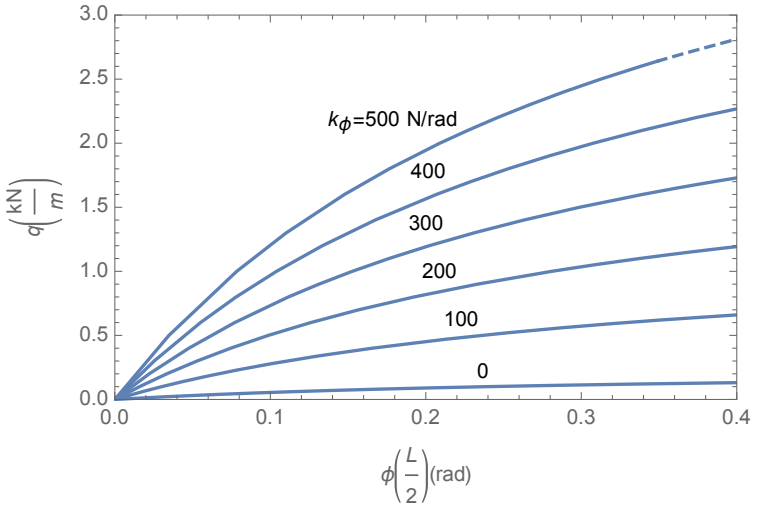

Figure 12: Gravity load versus central twist for Example 2 with $k_x = 0$

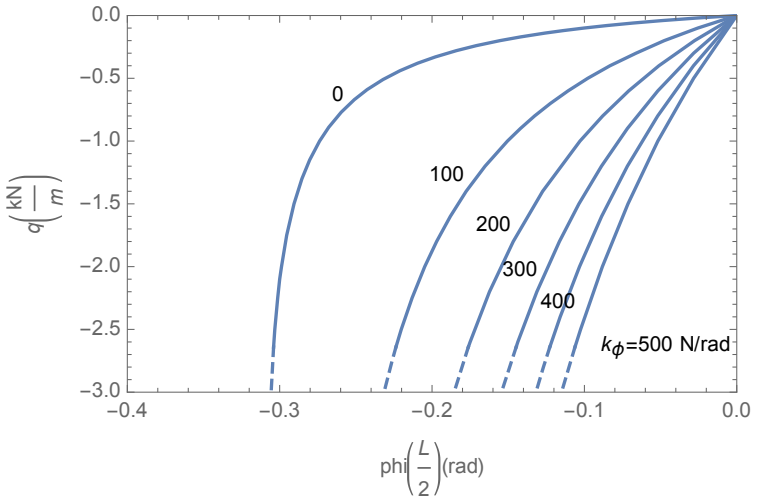

Figure 13: Uplift load versus central twist for Example 2 with $k_x = 0$

Results for the case $k_x = 0.1$ N/mm^2 are presented in Figs. 14 and 15, respectively, for gravity and uplift loading. The values of k_ϕ are 250, 500, 750, 1000, 1250, and 1500 N/rad. The range of q is 0 to 6 kN/m in Fig. 14, and –35 kN/m to 0 in Fig. 15. However, in Fig. 15 the maximum slope magnitude $|v'(0)|$ of the vertical deflection is larger than 0.3 if $q < -10.2$ kN/m for the bottom curve and if $q < -10.1$ kN/m for the other curves.

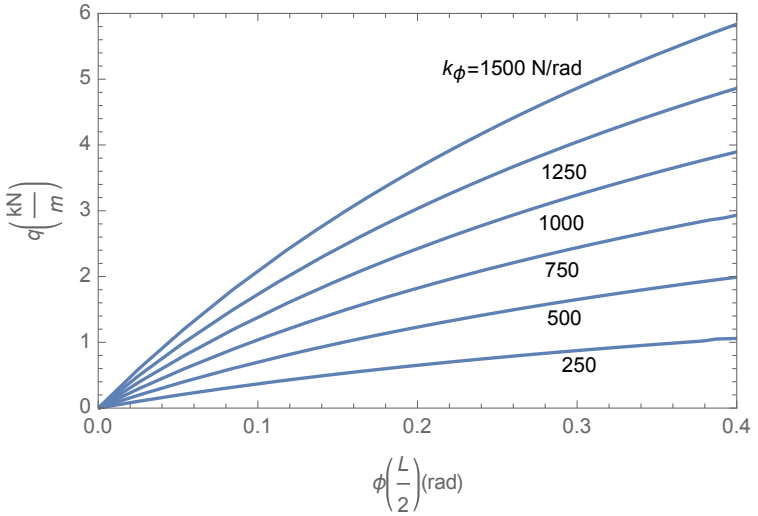

Figure 14: Gravity load versus central twist for Example 2 with $k_x = 0.1$ N/mm^2

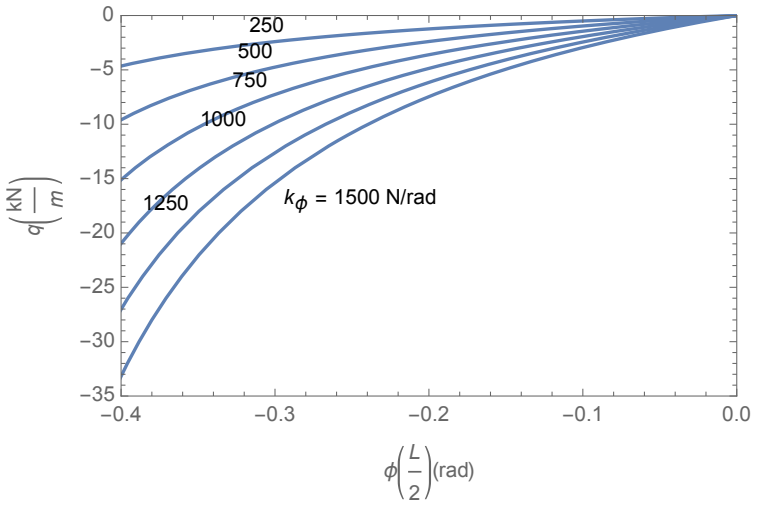

Figure 15: Uplift load versus central twist for Example 2 with $k_x = 0.1$ N/mm^2

In Figs. 16 and 17, there is no torsional restraint ($k_\phi = 0$). Curves for $k_x = 0$, 0.001, and 0.1 N/mm^2 are depicted in Fig. 16 for gravity loading. The curves intersect and are close to each other. For uplift loading in Fig. 17, curves for $k_x = 0$, 0.0002, 0.0005, 0.001, and 0.1 N/mm^2 are shown. The range of q is 0 to 0.15 kN/m in Fig. 16, and –4 kN/m to 0 in Fig. 17. As in Example 1, results for large lateral stiffnesses are close to those for $k_x = 0.1$ N/mm^2.

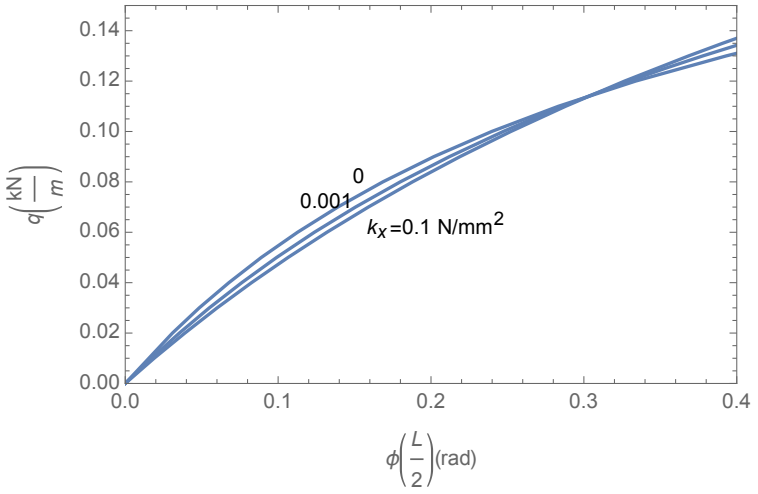

Figure 16: Gravity load versus central twist for Example 2 with $k_\phi = 0$

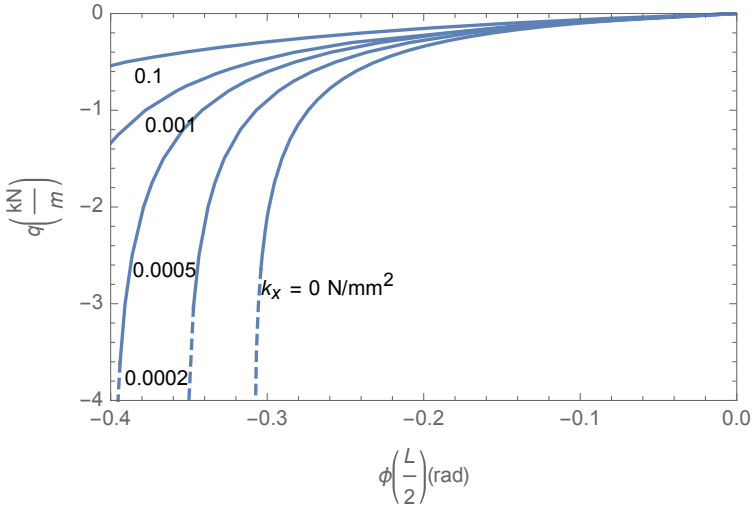

Figure 17: Uplift load versus central twist for Example 2 with $k_\phi = 0$

Fig. 18 depicts the shape of the twist $\phi(z)$ for the case q = –30 kN/m, k_x = 0.1 N/mm^2, and k_ϕ = 1500 N/rad. The maximum magnitude of the twist does not occur at the center of the beam in this atypical case.

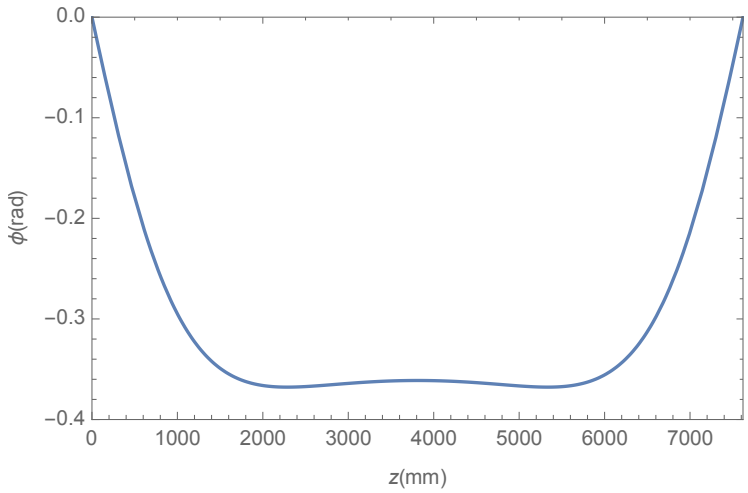

Figure 18: Shape of twist for Example 2 with q = –30 kN/m, k_x = 0.1 N/mm^2, and k_ϕ = 1500 N/rad

Finally, k_ϕ = 1000 N/rad in Figs. 19 and 20, with curves plotted for k_x = 0, 0.0005, 0.001, 0.003, 0.01, and 0.1 N/mm^2. The range of q is 0 to 6 kN/m in Fig. 19, and –25 kN/m to 0 in Fig. 20. In Fig. 20, the magnitude of $|v'(0)|$ is greater than 0.3 for k_x = 0.1, 0.01, and 0.003 N/mm^2, respectively, if $q < -10.1$, –9.2, and –7.9 kN/m.

Comparing these figures to Figs. 10 and 11 having the same rotational stiffness, it is seen that changes in k_x have a greater effect for Example 2 than for Example 1.

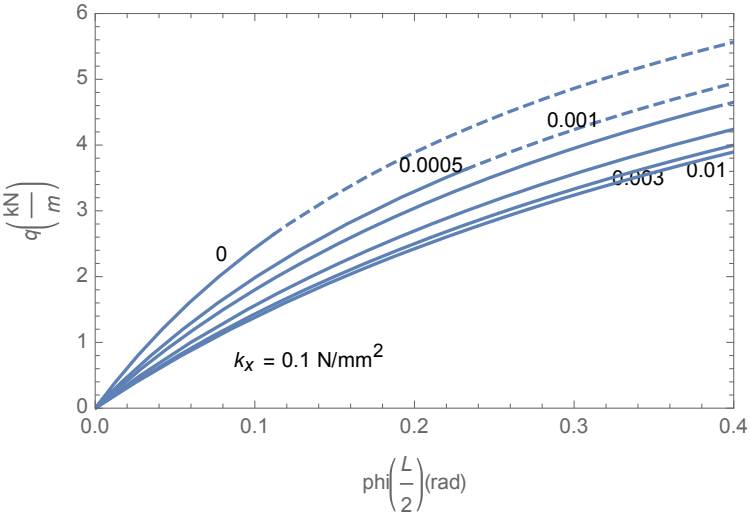

Figure 19: Gravity load versus central twist for Example 2 with k_ϕ = 1000 N/rad

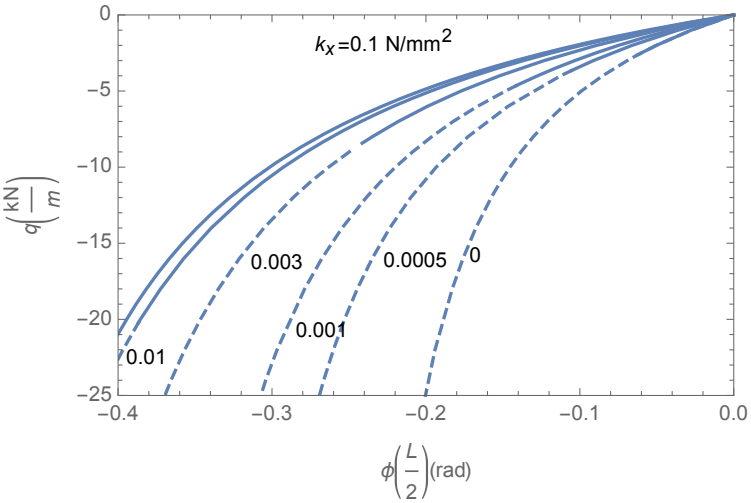

Figure 20: Uplift load versus central twist for Example 2 with k_ϕ = 1000 N/rad

5. Examples 1 and 2 with Roof Slope

The effect of roof slope angle θ is considered now (see Fig. 2). Numerical results will be presented for the range –0.5 $\leq \theta \leq$ 0.5 where θ is in radians. A low slope with pitch 1:12 corresponds to θ = 0.083 rad = 4.76°, and a high slope with pitch 6:12 corresponds to θ = 0.46 rad = 26.57°. It is noted that θ is positive if counter-clockwise, whereas the beam twist ϕ is positive if clockwise (see Fig. 1).

Uplift pressure due to wind is perpendicular to the roof. Therefore it acts the same as wind uplift for the case when there is no roof slope, and the uplift results in Sections 3 and 4 are applicable.

For gravity loading, results are presented in Figs. 21-24. The twist $\phi(L/2)$ at the center of the beam is plotted as a function of the roof slope angle θ. Each curve has a maximum value of the

central twist at some positive value of θ (i.e., with the beam in an upslope orientation, as in Fig. 2).

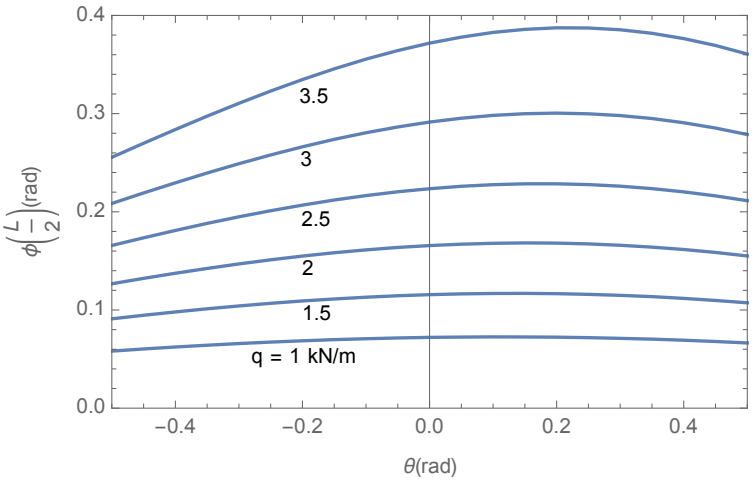

Figure 21: Central twist versus roof slope for Example 1 with k_x = 0.1 N/mm^2 and k$_\phi$ = 1000 N/rad

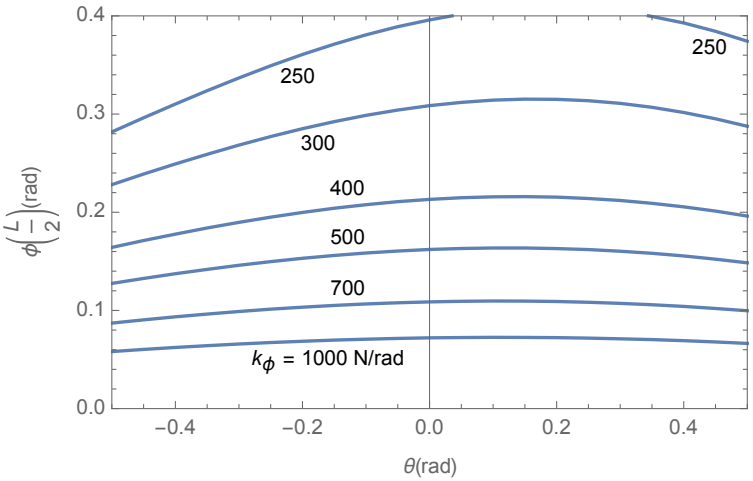

Figure 22: Central twist versus roof slope for Example 1 with q = 1 kN/m and k_x = 0.1 N/mm^2

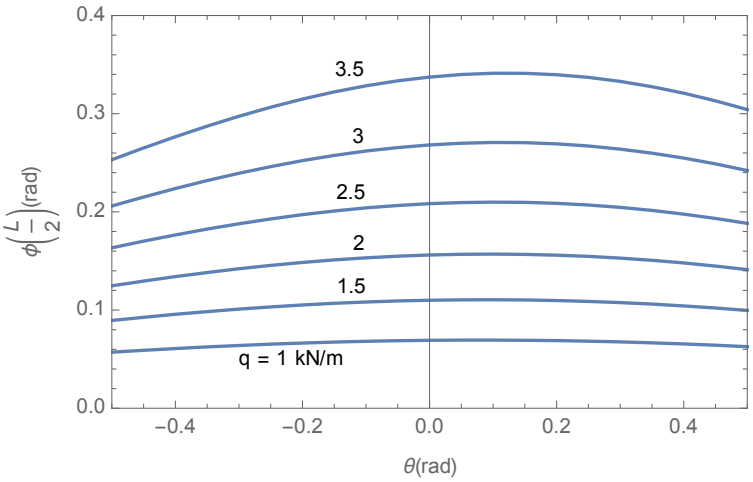

Figure 23: Central twist versus roof slope for Example 2 with k_x = 0.1 N/mm^2 and k$_\phi$ = 1000 N/rad

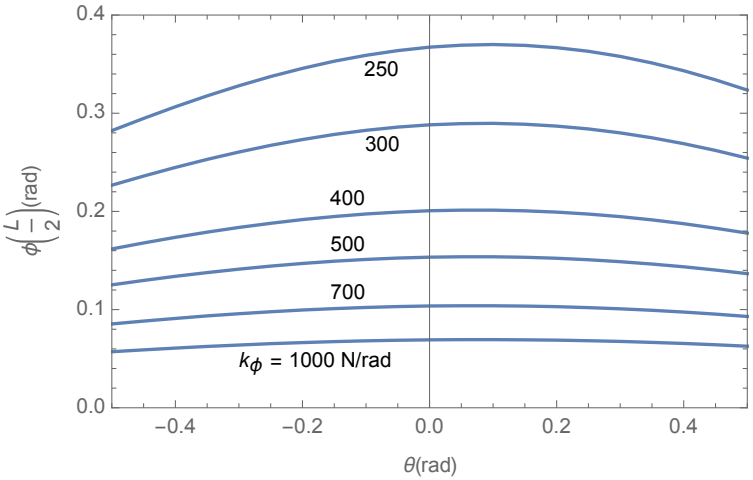

Figure 24: Central twist versus roof slope for Example 2 with q = 1 kN/m and k_x = 0.1 N/mm^2

Figs. 21 and 22 are associated with Example 1, and Figs. 23 and 24 with Example 2. In Figs. 21 and 23, k_x = 0.1 N/mm^2, k$_\phi$ = 1000 N/rad, and curves are plotted for q = 1, 1.5, 2, 2.5, 3, and 3.5 kN/m. In Figs. 22 and 24, q = 1 kN/m, k_x = 0.1 N/mm^2, and curves are plotted for k$_\phi$ = 250, 300, 400, 500, 700, and 1000 N/rad. As q decreases or k_ϕ increases, the effect of changes in the roof slope angle θ decreases (i.e., the curves become flatter).

6. Buckling

Consider global buckling for the case of no roof slope. (Local and distortional buckling are not considered in this paper.) Based on the linearly elastic behavior assumed here, lateral-torsional buckling (LTB) cannot occur for uplift because the compressed flange lateral deformations for the two (combined) loading actions, flexure and direct torsion, oppose each other.

6.1 C-Section Beams

For the C section in Fig. 1(a), LTB can occur under gravity loading if $a_x = q_x = 0$, with the vertical

load acting on an extension of the top flange, having its line of action pass through the shear center S. Equations (2) and (4) become homogeneous equations in $u(z)$ and $\phi(z)$, which are proportional to $sin(\pi z/L)$ at the critical load $q = q_{cr}$ given by

$$q_{cr} = \frac{1}{a_y}\left[k_\phi + rGJ + r^2E\left(C_w + \frac{{a_y}^2 I_y k_x}{k_x + r^2 E I_y}\right)\right] \tag{6}$$

where $r = (\pi/L)^2$.

If the parameters for Example 1 are used in Eq. (6), the resulting value of q_{cr} is the horizontal asymptote for curves such as those in Figs. 4 and 6 (i.e., the value of q would approach q_{cr} if the horizontal axis were extended to very high values). One can also relate q_{cr} to the problem treated in Section 3 by plotting q/q_{cr} as a function of the central twist, which is shown in Fig. 25 for k_x = 0.1 N/mm^2. Curves are plotted for k_ϕ = 0 and 1500 N/rad, and results for rotational stiffnesses between these values lie in the narrow band between the two curves. To apply Fig. 25, for example, if k_x = 0.1 N/mm^2 and k_ϕ = 0, the load that would cause $\phi(L/2) = 0.4$ rad is $q = 0.381 q_{cr}$ = (0.381)(0.399 kN/m) = 0.152 kN/m.

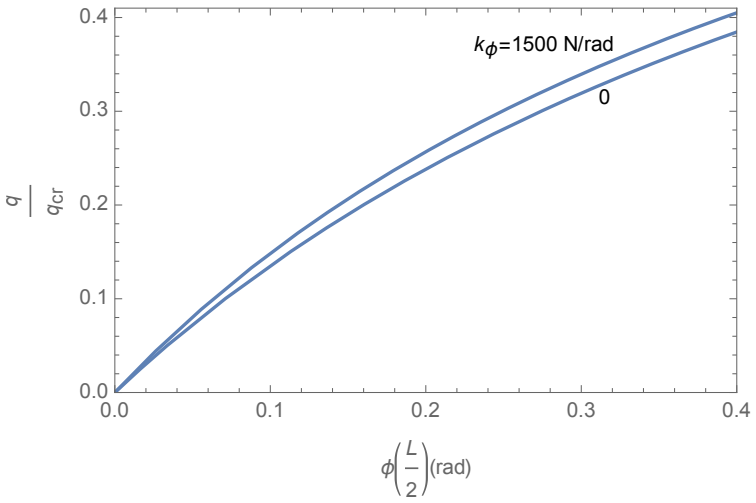

Figure 25: Ratio q/q_{cr} versus central twist for Example 1 with gravity loading and k_x = 0.1 N/mm^2

6.2 Z-Section Beams

For the Z section in Fig. 1(b), LTB can occur under gravity loading if there is no lateral spring (k_x = 0) and if the load acts along the major principal axis, which requires the load to be angled (see Fig. 2) with its line of action passing through S. The angle α of the principal axes relative to the x and y axes in Fig. 1 is found from $tan(2\alpha) = -2I_{xy}/(I_x – I_y)$ (Beer et al. 2019). For Example 2, this yields $|\alpha|$ = 0.278 rad, and the angled load is located at a_x = 29.049 mm (1.144 in.), slightly larger than the value of a_x in Section 4.

For Example 2 with k_x = 0 and the downward load acting along the major principal axis, the critical load for LTB is

$$q_{cr} = \frac{k_\phi + rGJ + r^2 EC_w}{\sqrt{a_x^2 + a_y^2}} \tag{7}$$

where $r = (\pi/L)^2$. It increases linearly with k_ϕ. Curves for k_ϕ = 0 and 1500 N/rad are shown in Fig. 26, similarly to Fig. 25. As an example, if $k_x = k_\phi = 0$, the load that would cause $\phi(L/2) =$ 0.4 rad is $q = 0.554 q_{cr}$ = (0.554)(0.236 kN/m) = 0.131 kN/m.

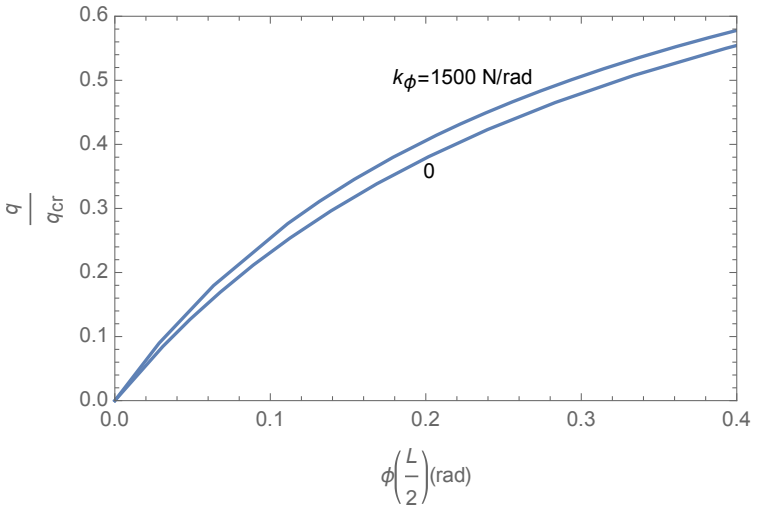

Figure 26: Ratio q/q_{cr} versus central twist for Example 2 with gravity loading and $k_x = 0$

7. Concluding Remarks

Lateral-torsional deformations of partially restrained, single-span, simply-supported C-section and Z-section beams were investigated. On the top flange, the beams were subjected to distributed loading (gravity or uplift) and to elastic restraints modeled as distributed lateral and rotational springs.

It was assumed that the beam and restraints were linearly elastic, and that the deformations were small. Distortion of the cross section was neglected. The equilibrium equations were presented and were solved numerically. Results for the two examples demonstrated the effects of load magnitude, lateral and torsional restraint stiffnesses, and roof slope on the twist at the center of the beam.

Naturally, the stiffness of the torsional restraint tended to have a large effect on the twist. In some cases, the lateral stiffness had little influence on the twist (see Figs. 10, 11, and 16). For $k_x >$ 0.1 N/mm^2, additional lateral stiffness has little effect. As the roof slope was varied from a high downslope configuration to being flat and then to a high upslope configuration, the maximum twist occurred for a slight upslope.

In Section 6, the concept of a critical load was considered for the case of no roof slope. The linearly elastic analysis used in this paper, with the load applied at the midpoint of the top flange of a C-section or Z-section beam, does not lead to any buckling. For a modified loading (vertical gravity load acting through the shear center for a C-section beam, or acting with a particular location

and angled orientation for a Z-section beam with no lateral bracing), lateral-torsional buckling can occur. Relations between the maximum twist for the actual loading and the associated critical load for the modified loading were discussed.

References

AISI (2017). Cold-Formed Steel Design Manual, American Iron and Steel Institute, Washington, DC.

Bai, F., Yang, N., Zhang, H., and Wang, X. (2018). "A modified direct strength method for nonlinear twisting model of simply-supported C-section purlins," Journal of Constructional Steel Research, 150, 384-391.

Balázs, I., and Melcher, J. (2017). "Influence of uplift load on torsional restraint provided to thin-walled purlins by sandwich panels," Procedia Engineering, 190, 35-42.

Balázs, I., Melcher, J., and Belica, A. (2017). "Experimental investigation of torsional restraint provided to thin-walled purlins by sandwich panels under uplift load," Procedia Engineering, 161, 818-824.

Beer, F. P., Johnston, E. R., and Mazurek, D. (2019). Vector Mechanics for Engineers: Statics, 12th edition, McGraw-Hill, New York.

Chu, X.-T., Kettle, R., and Li, L.-Y. (2004). "Lateral-torsion buckling analysis of partial-laterally restrained thin-walled channel-section beams," Journal of Constructional Steel Research, 60, 1159-1175.

Chu, X.-T., Rickard, J., and Li, L.-Y. (2005). "Influence of lateral restraint on lateral-torsional buckling of cold-formed steel purlins," Thin-Walled Structures, 43, 800-810.

Chu, X.-T., Ye, Z.-M., Li, L.-Y., and Kettle, R. (2006). "Local and distortional buckling of cold-formed zed-section beams under uniformly distributed transverse loads," International Journal of Mechanical Sciences, 48, 378-388.

EN 1993-1-3 (2006). Eurocode 3: Design of steel structures - Part 1-3: General rules - Supplementary rules for cold-formed members and sheeting, European Committee for Standardization, Brussels, Belgium.

Gajdzicki, M. (2018). "Sheet-to-purlin fasteners arrangement and the value of rotational restraint of cold-formed Z-purlins," Journal of Constructional Steel Research, 151, 185-193.

Gajdzicki, M., and Goczek, J. (2015). "Numerical determination of rotational restraint of cold-formed Z-purlin according to EC3," International Journal of Steel Structures, 15, 633-645.

Gao, T., and Moen, C. D. (2012). "Predicting rotational restraint provided to wall girts and roof purlins by through-fastened metal panels," Thin-Walled Structures, 61, 145-153.

Gao, T., and Moen, C. D. (2014). "Extending the direct strength method for cold-formed steel design to through-fastened simple span girts and purlins with laterally unbraced compression flanges," Journal of Structural Engineering, 140, 04014010.

Gosowski, B., Kubica, E., and Rykaluk, K. (2015). "Analysis of laterally restrained cold-formed C-shape purlins according to Vlasov theory," Archives of Civil and Mechanical Engineering, 15, 456-468.

Katnam, K. B., Van Impe, R., Lagae, G., and De Strycker, M. (2007a). "Modelling of cold-formed steel sandwich purlin-sheeting systems to estimate the rotational restraint," Thin-Walled Structures, 45, 584-590.

Katnam, K. B., Van Impe, R., Lagae, G., and De Strycker, M. (2007b). "A theoretical numerical study of the rotational restraint in cold-formed steel single skin purlin-sheeting systems," Computers and Structures, 85, 1185-1193.

Katnam, K. B., Van Impe, R., Lagae, G., and De Strycker, M. (2008). "Design of cold-formed steel purlins attached to roof sheeting based on Eurocode 3: Effect of gravity load," Advances in Structural Engineering, 11, 199-208.

Khelil, A., and Larue, B. (2008). "Simple solutions for the flexural-torsional buckling of laterally restrained I-beams," Engineering Structures, 30, 2923-2934.

Kujawa, M., and Szymczak, C. (2014). "Numerical and experimental investigation of rotational stiffness of zed-purlins connection with sandwich panels," Thin-Walled Structures, 75, 43-52.

Lei, J.-S., and Li, L.-Y. (2017). "Combined web distortional and lateral-torsional buckling of partially restrained I-section beams," International Journal of Mechanical Sciences, 131-132, 107-112.

Li, L.-Y. (2004). "Lateral-torsional buckling of cold-formed zed-purlins partial-laterally restrained by metal sheeting," Thin-Walled Structures, 42, 995-1011.

Li, L.-Y., Ren, C., and Yang, J. (2012). "Theoretical analysis of partially restrained zed-purlin beams subjected to up-lift loads," Journal of Constructional Steel Research, 70, 273-279.

Lucas, R. M., Al-Bermani, F. G. A., and Kitipornchai, S. (1997). "Modelling of cold-formed purlin-sheeting systems - Part 2: simplified model," Thin-Walled Structures, 27, 263-286.

Moen, C.D. (2020). Design Example - Four Span Continuous Z-Purlins Attached to a Standing Seam Roof <https://nextjournal.com/runtosolve/metal-building-standing-seam-roof-example> (accessed January 13, 2020).

Penava, D. S., Damjanović, D., and Ilijaš, T. (2015). "The impact analysis of lateral restraint on the state of stress in the thin-walled Z-section beam," Transactions of FAMENA, 39, 1-14.

Plaut, R. H., and Moen, C. D. (2019). "Flexural-torsional deformations of imperfect thin-walled columns with continuous bracing," Proceedings of the 2019 SSRC Annual Stability Conference, St. Louis, MO, April 22-25, 2019.

Ren, C., Li, L.-Y., and Yang, J. (2012). "Bending analysis of partially restrained channel-section purlins subjected to up-lift loadings," Journal of Constructional Steel Research, 72, 254-260.

Ren, C., Zhao, X., and Chen, Y. (2016). "Buckling behaviour of partially restrained cold-formed steel zed purlins subjected to transverse distributed uplift loading," Engineering Structures, 114, 14-24.

Seek, M. W., and Escobales, N. (2016). "Computational procedure for normal stresses in C-sections and Z-sections with one flange attached to sheathing," Journal of Structural Engineering, 142, 04015143.

Seek, M. W., and Murray, T. M. (2008). "Lateral restraint forces in Z-section roof systems using the component stiffness method," Journal of Constructional Steel Research, 64, 1366-1378.

Tang, Y., Tong, G., and Zhang, L. (2018). "Buckling of parallel purlins in standing seam or screw-fastened roofs," Thin-Walled Structures, 132, 136-150.

Virgin, L. N., Giliberto, J. V., and Plaut, R. H. (2018). "Deformation and vibration of compressed, nested, elastic rings on rigid base," Thin-Walled Structures, 132, 167-175.

Vrany, T. (2006). "Effect of loading on the rotational restraint of cold-formed purlins," Thin-Walled Structures, 44, 1287-1292.

Wang. F., Zhang, H., Yang, J., Bai, L., and Ren, C. (2018). "Numerical studies of the rotational stiffness of purlin-sheeting system," International Journal of Steel Structures, 18, 719-733.

Wu, X.-F., Zhao, Y.-H., Zhu, J., Sun, C., and Xie, C. (2014). "Buckling analysis of C-section cold-formed steel purlins under uplift loadings," Applied Mechanics and Materials, 627, 124-128.

Yang, N., and Bai, F. (2017). "Damage analysis and evaluation of light steel structures exposed to wind hazards," Applied Sciences, 7, app7030239.

Ye, Z.-M., Kettle, R. J., Li, L.-Y., and Schafer, B. W. (2002). "Buckling behavior of cold-formed zed-purlins partially restrained by steel sheeting," Thin-Walled Structures, 40, 853-864.

Ye, Z.-M., Kettle, R., and Li, L.-Y. (2004). "Analysis of cold-formed zed-purlins partially restrained by steel sheeting," Computers and Structures, 82, 731-739.

Yuan, W.-B., Cheng, S., Li, L.-Y., and Kim, B. (2014). "Web-flange distortional buckling of partially restrained cold-formed steel purlins under uplift loading," International Journal of Mechanical Sciences, 89, 476-481.

Zhang, L., and Tong, G.-S. (2016). "Lateral buckling of simply supported C- and Z-section purlins with top flange horizontally restrained," Thin-Walled Structures, 99, 155-167.

Zhao, C., Yang, J., Wang, F., and Chan, A. H. C. (2014). "Rotational stiffness of cold-formed steel roof purlin-sheeting connections," Engineering Structures, 59, 284-297.

Zhu, J., Chen, J.-K., and Ren, C. (2014). "Numerical study on the moment capacity of zed-section purlins under uplift loading," Structural Engineering and Mechanics, 49, 147-161.